Linear shaped-charge jet optimization using machine learning methods

D. M. Sterbentz, C. F. Jekel, D. A. White, J. L. Belof

March 31, 2023

Linear shaped-charge jet optimization using machine learning methods

Dane M. Sterbentz,[a)] Charles F. Jekel, Daniel A. White, Robert N. Rieben, and Jonathan L. Belof[b)]
Lawrence Livermore National Laboratory, Livermore, CA 94550, USA

Linear shaped charges are used to focus energy into rapidly creating a deep linear incision. The general design of a shaped charge involves detonating a confined mass of high explosive (HE) with a metal-lined concave cavity on one side to produce a high velocity jet for the purpose of striking and penetrating a given material target. This jetting effect occurs due to the interaction of the detonation wave with the cavity geometry, which produces an unstable fluid phenomenon known as the Richtmyer–Meshkov instability and results in the rapid growth of a long narrow jet. We apply machine learning and optimization methods to hydrodynamics simulations of linear shaped charges to improve the simulated jet characteristics. The designs that we propose and investigate in this work generally involve modifying the behavior of the detonation waves prior to interaction with the liner material. These designs include the placement of multiple detonators and the use of metal inclusions within the HE. We are able to produce a linear shaped-charge design with a higher penetration depth than the baseline case that we consider and accomplish this using the same amount of or less HE.

Keywords: Richtmyer–Meshkov instability, detonation waves, shock waves, shaped charges, optimization, machine learning

I. INTRODUCTION

Shaped charges are used in a variety of applications for creating deep incisions or perforations in hard, dense materials such as stone and metal. Depending on the intended use, the geometry of a shaped charge can take several forms including a radially symmetric (e.g., a conical shape) or linear configuration (i.e., with linear planar symmetry). Linear shaped charges are used to create deep linear cuts and have many commercial applications in industries including mining, oil and gas extraction/transmission, structural demolition, and rocket systems[1–3]. As a specific example, a linear shaped charge can be used to quickly sever oil or natural gas pipelines, which may be necessary during an emergency scenario[4]. Linear shaped charges are also used for rapid stage separation in multistage rocket systems for spacecraft launch vehicles[5,6].

Most linear shaped-charge designs involve encasing some type of high explosive (HE) in a shell of metal or other material. The casing is open on one side with a concave cavity cut into the HE material. This cavity is usually lined with a thin material that we subsequently refer to as the liner. A detonator (or detonators) is used to ignite the HE, which produces a detonation wave that travels through the HE to the liner. When this detonation wave reaches and interacts with the liner, it produces a Richtmyer–Meshkov instability that manifests as the liner material in the cavity begins to invert and is pulled into a narrow high-velocity jet that forms at the central apex of the liner cavity[7–9]. This phenomenon is also sometimes referred to as the Munroe or Neumann

effect[10]. Much of the hydrodynamic theory describing the process of liner jet formation was laid out by Birkhoff et al.[10] and Pugh et al.[11], whose work provides an analytical basis for this phenomenon and the penetrative properties of the jet. For many applications, it is desirable for this jet to strike a target (i.e., the material in which an incision is to be made) and penetrate as deeply as possible into this target, which is located at some specified distance from the linear shaped charge.

Work conducted by a number of researchers[12–17] has demonstrated that detonation wave properties can be modified and controlled to alter jetting and penetration properties for various types of shaped charges. Our work investigates several linear shaped charge design parameterizations using two-dimensional hydrodynamics simulations and design optimization methods. We use these design parameterizations to modify properties of the HE detonation waves prior to interaction with the liner material with the goal of altering jet characteristics to increase the penetration depth into a given material target. We run numerous simulations in parallel on a high performance computer (HPC) to generate large datasets. These datasets are then used to train neural network models for use as a surrogate to aid in iteratively optimizing the penetrative properties of the jet. In our analysis, we generally leave the liner angle, thickness, and material unchanged, as these properties have been somewhat extensively studied in previous works[18–23].

Our parameterizations include altering the positions of multiple detonators and the addition of metal inclusions within the HE. We provide justification for the selection of these design parameterizations using analytical expressions that describe the dynamics of detonation wave interactions, such as the pressure increase from the collision of detonation waves[13,24,25]. Due to the high computational time cost of simulating the penetration of a jet into a target, we also investigate potential optimiza-

a)Electronic mail: sterbentz2@llnl.gov
b)Electronic mail: belof1@llnl.gov

tion metrics that correlate to penetration depth[10,26], but do not require us to fully simulate the penetration of the jet into a target. This is particularly useful for our optimization analysis that involves conducting numerous hydrodynamics simulations. From our analysis, we produce several optimized linear shaped-charge designs with a higher penetration depth than the baseline case and, in some cases, accomplish this using less HE.

II. METHODOLOGY

A. Hydrodynamics simulation setup

The configuration, including dimensions, of our two-dimensional hydrodynamics simulation for the baseline case that we compare to our optimized designs is shown in Figure 1. Our two-dimensional simulation configuration has linear planar symmetry boundary conditions and extends infinitely in the z-direction out of the page. The linear shaped charge in this configuration consists of HE surrounded by a stainless steel casing. On the open side of the HE, an angled cavity protrudes into the HE and is lined with copper. The liner angle that we use for most of our simulations is $\alpha = 60°$. In front of the liner, we use air at ambient conditions (i.e., atmospheric pressure and room temperature). A single detonator is placed near the back of the HE region, which is used to initiate the detonation wave that strikes the copper liner. Note that the air region extends further than what is shown in Figure 1 and the total length of the simulation in the x-direction is equal to 10 cm.
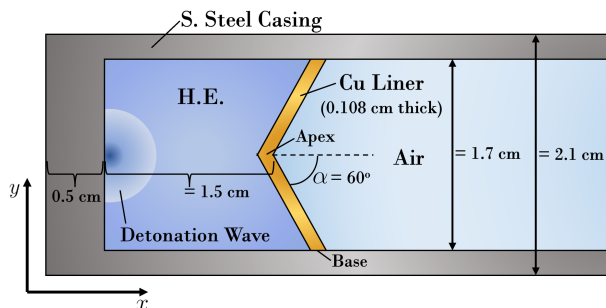

FIG. 1: The linear shaped-charge configuration that we use in our simulations for the baseline case. The materials used and their corresponding locations and dimensions are marked on the diagram. This configuration involves linear planar symmetry and extends infinitely in the z-direction (i.e., out of the page).

We construct these simulations using the MARBL hydrodynamics code[27,28]. MARBL is an arbitrary Lagrangian–Eulerian code that uses a high-order finite element method to solve the conservation of mass, momentum, and energy equations[29]. Our simulation mesh has approximately 10,600 elements, with higher mesh re-

finement in the HE and liner region and along the path of the jet. These elements are quadratic for kinematic fields and piecewise-discontinuous linear for thermodynamic fields. Our simulations also output a density and a velocity field image on a fixed Cartesian grid at equally spaced time steps throughout the simulation using the Ascent software library[30]. We use these Ascent images to calculate the fitness metric for our optimization analysis, which is described further in Section II C.

The materials in our simulations are modeled using the Livermore Equation of State (LEOS) library. The material equations of state for copper, stainless steel, and air, come from LEOS tables 290[31], 3010, and 2260, respectively. They are based on the quotidian equation of state with extension formalism[32,33]. For the copper and stainless steel in our simulations, we use the Steinberg–Guinan strength model[34]. For the copper strength model, we use a shear modulus of 0.477 Mbar, an initial yield stress of 1.2×10^{-3} Mbar, and a maximum work hardening stress of 6.4×10^{-3} Mbar. Similarly, for the stainless steel strength model, we use a shear modulus of 0.770 Mbar, an initial yield stress of 3.3×10^{-3} Mbar, and a maximum work hardening stress of 2.5×10^{-3} Mbar. To simulate the detonation and combustion dynamics of the HE, we use a reactive flow model[35–37], which has the ability to account for a broad range of detonation and shock phenomena not captured by programmed burn models[38,39]. We neglect the strength of the unreacted HE in our simulations.

B. Jet formation dynamics

The unstable fluid motion that occurs when a shock or detonation wave interacts with an interface between two materials is known as the Richtmyer–Meshkov instability (RMI) and often results in high-velocity jetting when the interface includes a cavity, groove, or other non-flat perturbation[7–9]. This jetting behavior is sometimes referred to as the Munroe effect when it occurs in shaped-charge applications. Although the liner is a solid material (e.g., copper), the high stresses in shaped-charge detonations tend to exceed the yield stress of the liner material, which implies that the liner jet formation can largely be approximated using fluid mechanics. The following equation provides a simple relation that describes the velocity at an RMI jet tip for scenarios where the materials involved can be approximated as fluids and the perturbation at the interface is approximately sinusoidal[7,8]:

$$v_\mathrm{j} = k\eta_0 A \Delta u_p, \tag{1}$$

where k is the wave number of the perturbation, η_0 is the initial amplitude of the perturbation, Δu_p is the jump in the particle velocity caused by the shock wave that strikes the perturbation (i.e., the shock wave that interacts with the liner–air interface in shaped-charge applications), and A is the Atwood number. When solid materials are involved, such as the case that we investigate

in this work, material elasticity and strength may also need to be considered. However, Equation (1) provides a general idea of what factors are important in producing a high-velocity jet.

The Atwood number A in Equation (1) plays a significant role in the behavior at the interface and is equal to

$$A = \frac{\rho_2 - \rho_1}{\rho_2 + \rho_1}, \tag{2}$$

where ρ_1 is the density of the upstream material (i.e., the liner material) and ρ_2 is the density of the downstream material (i.e., the air in front of the liner). For cases where $A < 0$, the liner cavity undergoes an inversion or collapse as the RMI jet begins to form. The original liner configuration (prior to being struck by the detonation wave) is shown in Figure 2(a). After the detonation wave strikes the liner, it induces RMI in the liner cavity which leads to the collapse or inversion of the liner as seen in Figure 2(b). Eventually the liner material will be entirely pulled into a high-velocity jet as shown in Figure 2(c). For the results that we show in this paper, we focus on the area within the rectangle shown in Figure 2(d), but we do account for the volume expansion that occurs around the HE region after the HE is detonated. Note that the color scales for all density and pressure plots in this paper are shown in Figure 3(a) and (b), respectively.

The work of Birkhoff et al.[10] was among the first to provide a strong analytical foundation for the fluid mechanics of the collapse of the liner and formation of the high-velocity jet. According to Birkhoff et al., a detonation wave with velocity u_d strikes the liner (with an original liner angle of α) and causes the liner to collapse (or invert slightly) to a new angle β where $\beta > \alpha$ (see Figure 4). Note that β is somewhat difficult to determine analytically because it depends on a number of factors including liner thickness, the liner angle α, the detonation wave velocity u_d, the angle from the vertical at which the detonation wave strikes the liner ω, etc. Vorticity deposition from the detonation wave and the collapse of the liner also causes the liner material to be pushed towards the central axis with a velocity of v_0, where it is expelled as both a jet with velocity v_j and a more slowly moving slug with velocity v_s[10,11,40]. Note that both v_j and v_s are in the same direction, but v_j is generally much greater than v_s. From the Birkhoff et al.[10,11] derivation, an approximation for the jet velocity v_j is given by

$$v_j = v_0 \csc\left(\frac{\beta}{2}\right) \cos\left(\alpha - \frac{\beta}{2} + \delta\right), \tag{3}$$

and an approximation for the slug velocity v_s is given by

$$v_s = v_0 \sec\left(\frac{\beta}{2}\right) \sin\left(\alpha - \frac{\beta}{2} + \delta\right), \tag{4}$$

where v_0 is the liner collapse velocity, which can be computed using

$$v_0 = \frac{2u_d}{\cos(\omega + \alpha)} \sin(\delta), \quad \omega + \alpha \leq \frac{\pi}{2}. \tag{5}$$
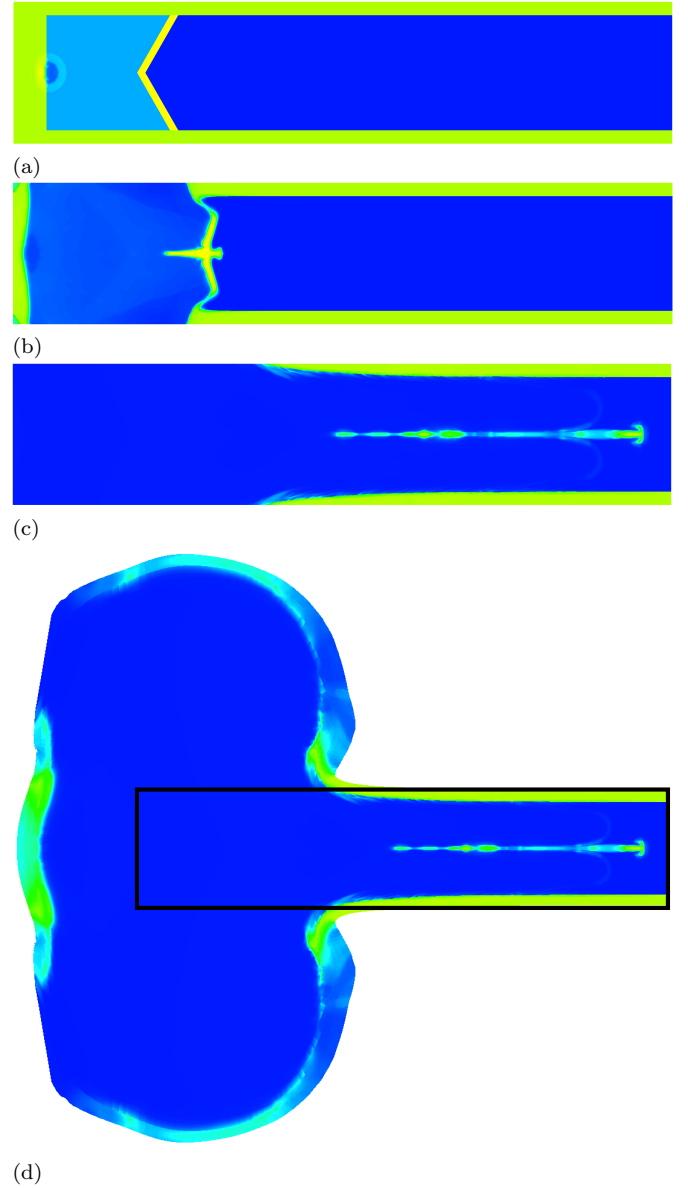

(a)

(b)

(c)

(d)

FIG. 2: Density plots for the baseline shaped-charge configuration that we consider in this study are shown at several time instants Δt after the HE detonator is ignited: (a) prior to detonation wave interaction with liner, $\Delta t = 0.3$ μs; (b) as liner begins to invert or collapse, $\Delta t = 5.0$ μs; (c) after jet has fully formed, $\Delta t = 20.0$ μs; (d) zoomed out showing volume expansion due to detonation of HE (area of interest is within black rectangle), $\Delta t = 20.0$ μs.

In Equation (5), ω is the angle of the detonation wave relative to the vertical and δ is the angle from the line normal to the liner angle along which a section of the liner moves. Note that $u_d/\cos(\omega + \alpha)$ corresponds to the velocity at which the detonation wave sweeps along parallel to the liner and reduces to the equation in Pugh et al.[11] when $\omega = 0$. According to the steady-state deriva-
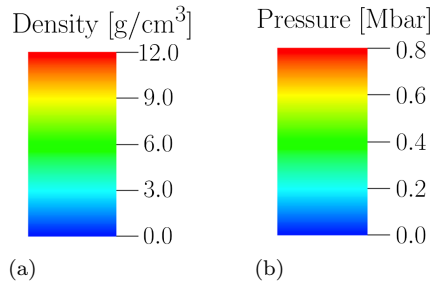
Density [g/cm^3]

Pressure [Mbar]

(a)

(b)

FIG. 3: The color scales that we use for density and pressure plots in this paper: (a) density [g/cm^3]; (b) pressure [Mbar].

tion given by Birkhoff et al., the angle δ is simply equal to

$$\delta = \frac{\beta - \alpha}{2}, \tag{6}$$

where the liner collapse angle β is held constant. For the steady-state case, Equation (6) can be substituted into Equations (7) and (8) to obtain

$$v_j = v_0 \csc\left(\frac{\beta}{2}\right)\cos\left(\frac{\alpha}{2}\right), \tag{7}$$

$$v_s = v_0 \sec\left(\frac{\beta}{2}\right)\sin\left(\frac{\alpha}{2}\right). \tag{8}$$

Birkhoff et al. also derive an approximation for the amount of mass deposited in the jet as a function of the angle β that is equal to

$$m_j = \frac{m}{2}[1 - \cos(\beta)], \tag{9}$$

and for the slug is equal to

$$m_s = \frac{m}{2}[1 + \cos(\beta)], \tag{10}$$

where m is the total mass of the liner. These relations predict that, for the limiting case where the detonation wave strikes the liner at a normal angle (i.e., $\omega = \pi/2 - \alpha$), the collapse angle $\beta = \alpha$ and the jet velocity v_j can be continually increased as the liner angle goes to zero (i.e., as $\beta = \alpha \to 0$)[10]. However, from Equation (9), it is clear that the mass of the jet m_j also approaches zero as $\beta \to 0$. This means that properties such as jet momentum and kinetic energy will not necessarily be increased as $\beta = \alpha \to 0$. This type of tradeoff between jet velocity v_j and jet mass m_j is a major challenge in shaped-charge design and optimization, where it is generally desirable for both of these quantities to be as high as possible.

While the analysis of Birkhoff et al. provides an excellent basis for understanding shaped-charge jet formation, it does overlook some important aspects of this process. For instance, the work of Pugh et al.[11] provides additional analysis on shaped-charge jet formation, such as
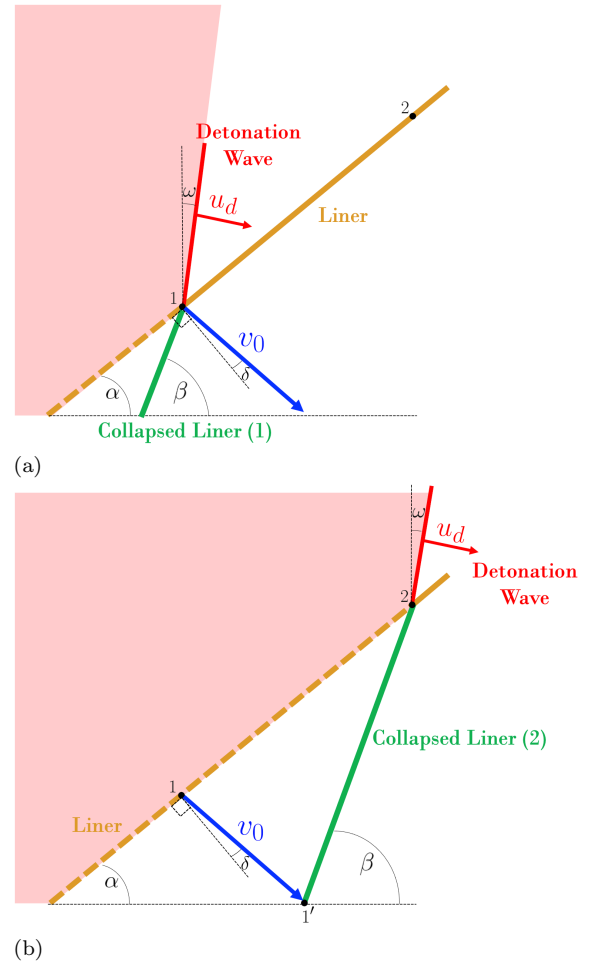

(a)

(b)

FIG. 4: These diagrams show the process of liner collapse as the detonation wave sweeps along the liner from the apex to the base. As time increases, the detonation wave moves from an arbitrary Point (1) to Point (2) as marked in the diagrams and the liner collapses from the original liner angle α to the liner collapse angle β. Several other variables involved in the analysis provided in the text are also marked on these diagrams including the detonation wave velocity u_d, collapse velocity v_0, the detonation wave angle ω, and the collapse velocity angle δ: (a) as the detonation wave passes through Point (1), the liner collapses and a velocity v_0 is imparted to the liner at Point (1) as described by Birkhoff et al.[10]; (b) the detonation wave continues to sweep along the liner and reaches Point (2). When the detonation wave reaches Point (2), Point (1) has moved to Point (1') where the liner mass at Point (1) is redirected horizontally into the jet.

accounting for variable collapse velocity v_0, to explain the large discrepancies between the Birkhoff et al. formulation and the jet length observed in experiments. The variable collapse velocity v_0 proposed by Pugh et al. implies that the collapse angle β (and consequently the angle δ) does not remain constant as the detonation wave
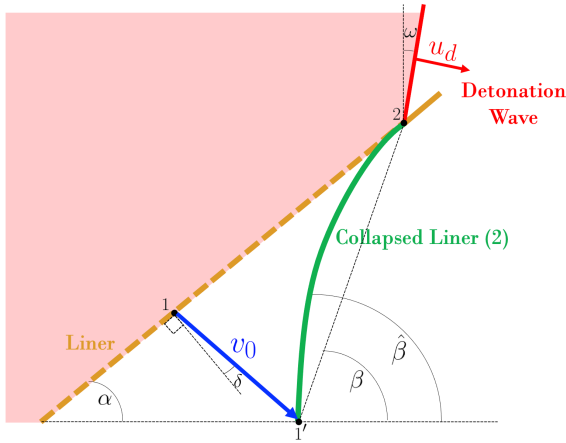
FIG. 5: For the idealized case in Figure 4(b), the liner collapse angle β remains constant. However, for most physical cases, the collapse velocity v_0 will vary along the length of the liner as collapse occurs, as described by Pugh et al.[11]. A variable collapse velocity v_0 consequently implies that the collapse angle β and collapse velocity angle δ will also vary. The diagram depicts the more physical case involving a variable collapse angle $\hat{\beta}$.

propagates from the liner apex to the liner base (i.e., the points where the liner contacts the outer casing). According to Pugh et al., even a small gradient or variation in the collapse velocity v_0 can produce a large gradient in the jet velocity v_j. This suggests that an optimal detonation wave angle ω may also change over time as the detonation wave sweeps along the liner from the apex to the base. Figure 5 shows an example of how β may vary as the detonation wave moves along the liner from apex to base.

This analytical theory provides an incentive for investigating different detonation wave front profiles where the angle ω can be varied along the detonation wave front, which allows us to find an optimal wave front for optimizing a penetration metric. While these analytical relations provide a reasonable starting point for understanding shaped-charge jet formation, hydrodynamics simulations are often needed to fully capture the flow dynamics present in the formation of the jet and slug. In the following sections, we describe our methodology for altering and shaping the detonation wave front with the objective of optimizing a fitness metric related to jet penetration depth into a target.

C. Optimization fitness metric

The ultimate goal of our optimization analysis is to increase the penetrative properties of the jet. While we can directly simulate the penetration of the shaped-charge jet into a target, this is computationally inefficient when running numerous simulations, such as for our optimization

analysis. Therefore, a correlation between penetration depth and a fitness metric based on more easily computable jet characteristics (e.g., jet velocity and density) is of great value. A fitness metric based on jet characteristics also allows us to use optimization methods to investigate how different designs influence these characteristics. A well-known analytical relation for predicting the penetration depth of the RMI jet was proposed by Birkhoff et al.[10] Several other empirical and analytical relations for predicting penetration depth, as well as other damage metrics, have also been proposed[26,41,42]. We start by considering the penetration depth relation proposed by Birkhoff et al.[10]

The relation proposed by Birkhoff et al. assumes a stationary reference frame moving at the penetration velocity U [i.e., the velocity at which the jet is penetrating into the target, see Figure 6(b)]. They also assume that the system reaches steady state instantaneously. Using these assumptions, Bernoulli's equation can be applied to obtain

$$\frac{1}{2}\rho_j(v_j - U)^2 = \frac{1}{2}\rho_t U^2, \quad (11)$$

where v_j is the jet velocity, ρ_j is the density of the jet, and ρ_t is the density of the target (see diagrams in Figure 6). Note that for the analysis in this section, we will no longer distinguish between jet and slug, but will simply refer to the entire mass (both slug and jet) as the jet, which has density ρ_j and velocity v_j. After some minor algebraic manipulation and assuming that the time it takes for penetration to occur is equal to $t_d = L/(v_j - U)$ where L is the total length of the jet mass (including the slug), the penetration depth d when the jet mass has fully struck the target is equal to

$$d = Ut_d = L\sqrt{\frac{\rho_j}{\rho_t}}. \quad (12)$$

This relation implies that the penetration depth is not directly a function of the jet velocity v_j, but is instead dependent on the length of the jet mass L. For a variable density jet $\rho_j(x)$, Equation (12) can be rewritten as

$$d = \frac{1}{\sqrt{\rho_t}} \int_0^L \sqrt{\rho_j(x)}dx, \quad (13)$$

where an integration is performed over the length of the jet. Since we are primarily interested in increasing the penetration depth regardless of the target material, we can remove ρ_t from the equation to obtain the following metric

$$\Phi_1 = \int_0^L \sqrt{\rho_j(x)}dx. \quad (14)$$

If we also consider the fact that the jet density is not constant in the y-direction, we can include a second integral, such that

$$\Phi_1 = \int_{-a}^a \int_0^L \sqrt{\rho_j(x,y)}dxdy, \quad (15)$$

where $-a$ and a are the bounds on the body of the jet in the y-direction. For our results, we simply set $a \approx 0.1$ cm. Alternatively, we found the following fitness metric to correlate more directly to the penetration depth in our simulations:

$$\Phi_2 = \int_{-a}^{a} \int_0^L \sqrt{\rho_j(x,y)} v_j(x,y) dxdy, \qquad (16)$$

where we have essentially just inserted the jet velocity v_j into the integral of Equation (15). The metric in Equation (16) has a kinetic energy analog given by

$$\Phi_3 = \frac{1}{2} \int_{-a}^{a} \int_0^L \rho_j(x,y) v_j(x,y)^2 dxdy, \qquad (17)$$

which correlates similarly to penetrative properties. However, we focus on the metric of Equation (16) in our optimization analysis.

(a)

(b)

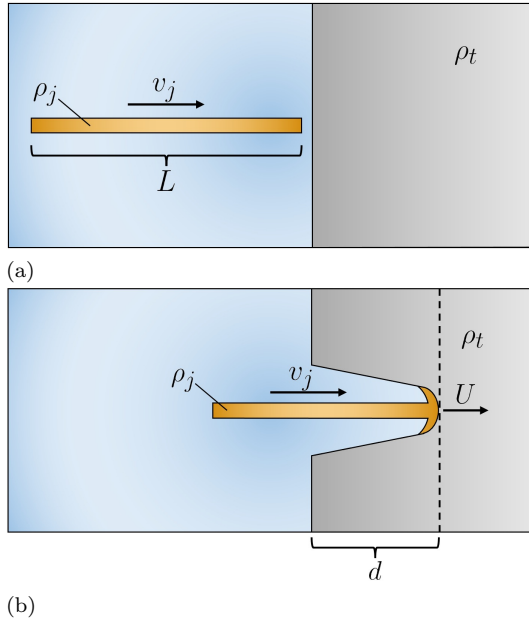FIG. 6: The shaped-charge jet can be approximated as a rod with density ρ_j and velocity v_j. When the jet strikes a target with density ρ_t, the jet penetrates into the target with a new velocity U up to a depth d. The diagrams in this figure show this process at two times: (a) just prior to the jet striking a target; (b) after the jet has penetrated a distance d into the target.

To assess these fitness metrics using our simulations, we include a tungsten target at a distance of 5.0 cm from the liner and use a parameterization in an array of simulations to vary the jet properties such that we obtain a variety of penetration depths. We use a tungsten target over other lower-density materials (e.g., steel) to reduce the time required for the jet to fully penetrate into the target and consequently reduce the time required to run these simulations. We then compute Φ_1 and Φ_2 for each simulation at a time just before the jet strikes the target.

We calculate these fitness metrics using images providing velocity and density fields that are output from our simulations using the Ascent software library[30], which are output at equally spaced time steps. The correlation between penetration depth into the target and the fitness metrics Φ_1 and Φ_2 are plotted in Figure 7(a) and (b), respectively. As can be seen in Figure 7, the fitness metric Φ_2 correlates much more strongly with penetration depth. The fitness metric Φ_1 may simply not be accurate enough for the shaped charge scenario that we consider. Therefore, for our optimization analysis, we compute Φ_2 as our fitness metric in place of simulating the penetration of the jet into a target. We also use the maximum value of the fitness metric over all time steps. While the stand-off distance between the liner and the target is an important parameter for determining penetration depth of a given jet, we are more concerned with finding the most penetrative jet at any stand-off distance occurring at any time throughout our simulation for our optimization analysis.

D. Optimization methodology

The fitness metrics Φ_1, Φ_2, and Φ_3 clearly depend upon the physics fields $v_j(x,y)$ and $\rho_j(x,y)$ evaluated at some physical time instant Δt. In addition, the physics state depends upon the initial design parameters, here defined as n independent scalar parameters $\mathbf{z} \in \mathcal{Z} = [0,1]^n \subset \mathbb{R}^n$. Thus, the fitness metrics are functions of the vector $\mathbf{z}$, and the design optimization problem is to find the best value of $\mathbf{z}$ given by

$$\max_{\mathbf{z} \in \mathcal{Z}} \Phi(\mathbf{z}), \qquad (18)$$

where we set $\Phi = \Phi_2$ for our analysis. We do not presume that the problem is convex, there can be multiple local maxima, therefore this is a global optimization problem. We do not have need for arbitrary constraints, as any manufacturing constraints are embedded into the design parameterization (discussed in section Section II E) below, hence this is an unconstrained global optimization problem. Note that, due to the nature of the physics simulation code MARBL that is used to perform the hydrodynamics simulations, derivative information $d\Phi(\mathbf{z})/d\mathbf{z}$ is not available. A lack of gradient information is not unique to MARBL, but is true of most hydrodynamics (and most multiphysics) codes. Code development for ALE hydrodynamics that provides gradient information is currently an open field of research. Therefore, we employ gradient-free (or "black-box") methods to solve this problem.

While there exists a great variety of gradient-free optimization methods, we employ a surrogate model based approach where the surrogate fitness metric is denoted by $\hat{\Phi}(\mathbf{z})$. This approach is data-driven, needing no information other than values of $\Phi(\mathbf{z})$ evaluated at selected sample points in $\mathcal{Z}$, but it results in a continuous approximate
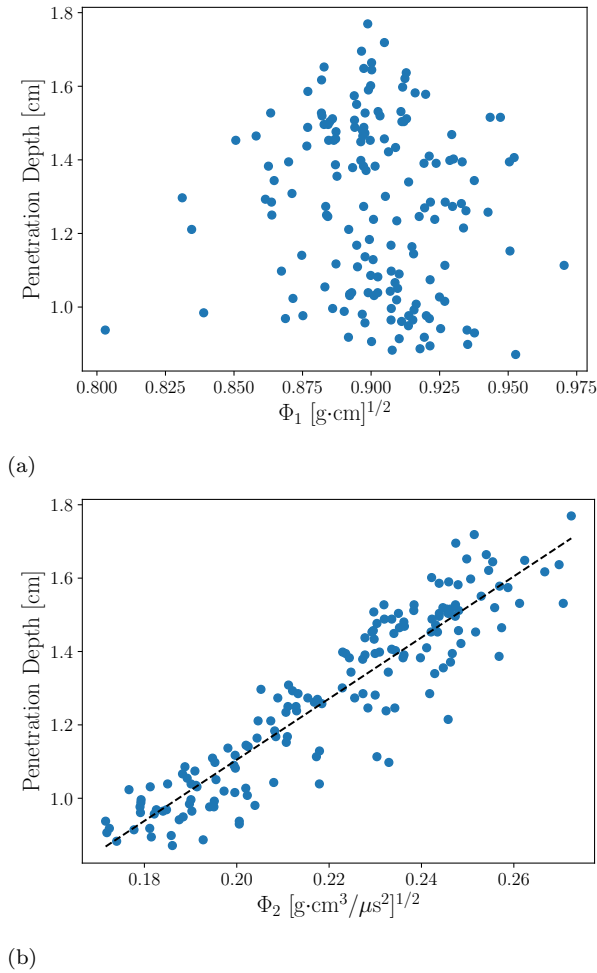
(a)

(b)

FIG. 7: Correlation between penetration depth into a tungsten target and two fitness metrics that we investigated in our study: (a) fitness metric Φ_1 given by Equation (15); (b) fitness metric Φ_2 given by Equation (16).

model that is useful for sensitivity analysis. Some excellent review articles on gradient-free optimization include those of Vu[43], Jones[44], Koziel[45], and Stork[46]. In order of increasing complexity, surrogate-based optimization may be based on polynomials, radial basis function interpolation, Gaussian process regression (a.k.a. Kriging), or artificial neural networks (ANN)[47]. The ANN approach is applied here, specifically a two hidden layer fully connected network using Gaussian activation functions[48]. The training can be done iteratively and the i-th iteration of the algorithm proceeds through the following general steps:

1. Define the sample domain $\mathcal{Z}_i$

2. Generate k_i sample points in $\mathcal{Z}_i$

3. Perform k_i hydrodynamics simulations

4. Compute k_i fitness metrics

5. Train ANN to learn the fitness metric as a function of the design variables to create surrogate model $\left(\mathbf{z}, \hat{\Phi}(\mathbf{z})\right)$

6. Use limited-memory Broyden–Fletcher–Goldfarb–Shanno (LBFGS) repeatedly from random starting points to find *all* the local maxima of $\hat{\Phi}(\mathbf{z})$

In this algorithm, convergence is defined as when the predicted optimal value of $\hat{\Phi}(\mathbf{z})$ agrees with the actual value of $\Phi(\mathbf{z})$ to within some tolerance (e.g., 5%).

It should be noted that in the literature many gradient-free optimization methods employ a combination of exploration (or diversification) and exploitation (or intensification). The approach described above is heavily weighted towards exploitation meaning that most random exploration is performed during the initial sampling and little subsequent random sampling is performed. As an example, for three design variables the initial exploration may consist of $3^5 = 243$ initial samples (we generally round this up to 300 samples), which is presumed to be a high enough sample density to have one sample in the neighborhood of the global optimum. Subsequent iterations then refine only the most promising regions of design space.

We perform the sampling in Step (1) using a traditional Latin hypercube. A traditional Latin hypercube is an n-dimensional sampling with two key properties: 1) a quasi-uniform space filling (no unusually large gaps between the samples); 2) non-collapsed, meaning that no coordinate is replicated. Latin hypercube samples are not unique, and finding the "best" set of samples can be a complicated optimization problem in itself. However, a traditional Latin hypercube gives us a reasonable sampling spread throughout much of the sample domain.

The hydrodynamics simulations performed in Step (3) can be performed in parallel. A scalable asynchronous task scheduler Merlin[49] is used to manage the workflow. This workflow scheduler runs all of the physics simulations, including the separate tasks of mesh generation, hydrodynamics, and the fitness metric post processing of Step (4). The machine learning in Step (5) utilizes the Pytorch library[50]. We use a fully connected two hidden layer network with Gaussian activation functions and 50 to 100 nodes for each hidden layer.

In Step (5) of the above algorithm, the well-known LBFGS algorithm is used to find all of the local maxima of the ANN model. The LBFGS algorithm is a quasi-Newton method, requiring gradients but not Hessians. The gradient of the model is easily computed using the built-in automatic differentiation capability of Pytorch. This method of course converges to a local maximum, and our goal is to find the global optimum. It is a simple matter to execute the LBFGS algorithm over and over again with $O(10^5)$ different starting points in the domain $\mathcal{Z}$. It must be noted that while a single hydrodynamics simulation may require 8 CPU hours, evaluation of the ANN model only requires approximately 0.1 seconds, so

this is not an expensive proposition. While no statistical proof is provided, it was observed that this approach found between 3 and 10 distinct local maximum thus the ANN model does not suffer from extreme oscillations and the global optimum of the ANN model is indeed found.

The above algorithm can be repeated multiple times where new samples are generated in a refined (or narrowed) sample domain within some fraction of the original domain centered at the global optimum found in the previous iteration (e.g., within $\pm 5\%$). However, we found that a single iteration followed by further simulations run within a refined sample domain (within $\pm 5\%$) was generally sufficient for our purposes. For a study with three design parameters, we typically use 300 hydrodynamics simulations in the first iteration and 100 further simulations in the refined sample domain. Each of our two-dimensional hydrodynamics simulations can be run in less than an hour on a single GPU (NVIDIA V100 on the Lassen HPC[51]). This constitutes the optimization methodology that we use. We apply this methodology to the design parameterizations described in the following section.

E. Design parameterizations

For our analysis, we investigate many different design parameterizations. However, for brevity, we will only focus on a few of the best performing parameterizations. The design parameterizations that we consider include altering the position of one or more detonators within the HE region, altering the time delay between the ignition of multiple detonators, and the addition of a metal inclusion (we use Cu for this purpose) within the HE region. When the HE detonation wave strikes the inclusion, it produces a shock wave that travels through the inclusion at a slower shock velocity u_s than the detonation wave velocity u_d. These parameterizations allow us to tune the detonation wave front to some degree and even split the detonation wave into multiple portions to induce detonation wave collisions.

The diagrams in Figure 8 show several sample designs that we investigate in our study. The parameterization in Figure 8(a) involves using three detonators, where two detonators are symmetrically placed about the central axis in the HE region and a third detonator is varied along the central axis in the x-direction. Figure 8(b) shows a parameterization that also involves three detonators, but introduces a time delay between the detonator on the central axis and the symmetric detonators (represented by different detonation wave radii in the diagram). The two symmetric detonators can be varied only along the stainless steel casing and the central detonator fixed near the edge of the casing. In this parameterization, either the two symmetric detonators or the central detonator can detonate first. The parameterization of Figure 8(c) involves using a copper inclusion in a triangular or chevron shape. As shown in the diagram, the dimensions

of the inclusion are varied, but symmetry about the central axis is maintained.
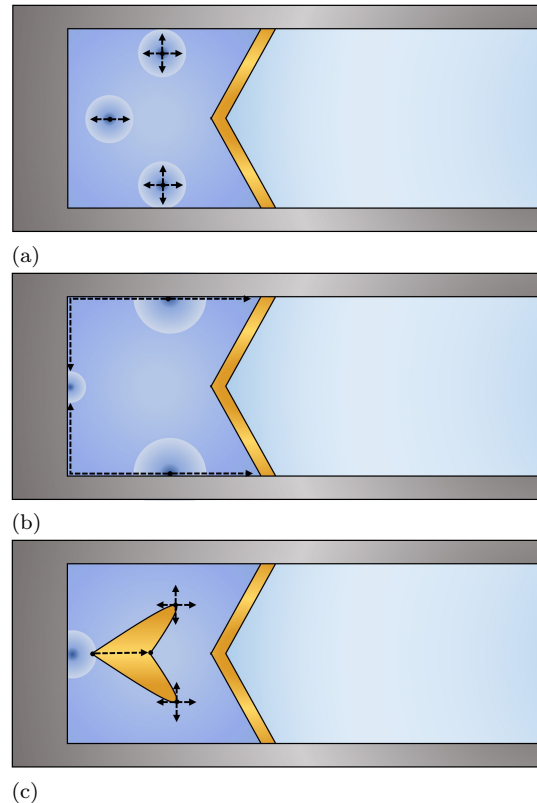

(a)

(b)

(c)

FIG. 8: Several samples of design parameterizations that we considered in our investigation; (a) three detonator design (detonators are ignited at the same time instant); (b) three detonator design where time delay is introduced between the ignition of the two symmetric detonators and ignition of the central detonator (either the two symmetric detonators or the central detonators can ignite first); (c) copper inclusion design in the shape of a chevron (note that this inclusion can take on a chevron, triangular, or diamond shape).

As previously mentioned, the design parameterizations that we have chosen allow us to modify the properties and shape of the detonation wave (or waves) that strike the copper liner. One phenomenon of particular interest is the localized increase in pressure that occurs due to collisions between detonation waves and whether this localized pressure increase is able to significantly affect properties of the resulting jet. The work of Zhang et al.[25] demonstrates that the locations of detonation wave collisions can be used to predict where fractures form along a steel plate coupled to HE with an array of detonators. Liu et al.[13] have also investigated the collision of detonation waves in relation to shaped charges applications. The maximum pressure in the collision region P_2 (i.e., the region where the detonation waves collide and overlap) relative to the original pressure of the individual

detonation waves P_1 can be correlated to the incidence angle ϕ_0 between two symmetric converging detonation waves. An analytical expression for the ratio P_2/P_1 is derived using the Rankine–Hugoniot jump conditions in Appendix A. In Appendix A, we also plot P_2/P_1 versus incidence angle ϕ_0 for a range of heat capacity ratios γ for different types of HE. We hypothesize that we may be able to enhance jetting by taking advantage of this phenomenon.

III. RESULTS AND DISCUSSION

In the following paragraphs, we present optimal results for several of our design parameterizations obtained using the optimization methodology described in Section II D. Figure 9 shows a density plot for an early time "initial" state for each of the design parameterizations that we present. Figure 9(a) shows the baseline case with a single detonator centered at the left of the HE region. Figure 9(b), (c), and (d), show the optimal initial states for the design parameterizations described in Figure 8(a), (b), and (c), respectively. Density plots at a time just prior to the detonation wave striking the liner are shown in Figure 10 for the same parameterizations as in Figure 9. Velocity vectors where the size of the vector corresponds to magnitude are overlaid on the plots in Figure 10. Pressure plots for the baseline case and for each of the design parameterizations are shown in Figure 11.

Ultimately, the optimal designs from several of our parameterizations produce very similar detonation wave fronts. This appears to be a case of "convergent evolution" where our vastly different parameterizations produce the same outcome when optimized. This wave front can be seen for three different parameterizations in Figure 11(b)–(d), where the front is slightly concave as opposed to the convex wave front seen in the baseline case in Figure 11(a). Localized high-pressure regions along the wave front can also be observed in Figure 11(b)–(d). These high-pressure regions along the wave front correspond to collisions between distinct detonation waves. These distinct detonation waves either emanate from the detonators or for the case in Figure 11(d) have been "split" into distinct waves by the metal inclusion. However, these high-pressure regions appeared to have a fairly minor effect on jetting properties. This is likely due to the fact that these high pressure regions are very localized and do not affect liner collapse velocity outside of a relatively small area. Further discussion on the effect of detonation wave collisions is provided later in this section and in Appendix A.

Density plots of jets produced by the baseline case and for an optimal case are shown in Figure 12(a) and (b), respectively. The optimal jet in Figure 12(b) has a longer length, higher tip velocity, and more of the mass is concentrated towards the front of the jet than the baseline jet in Figure 12(a). All of these properties contribute to
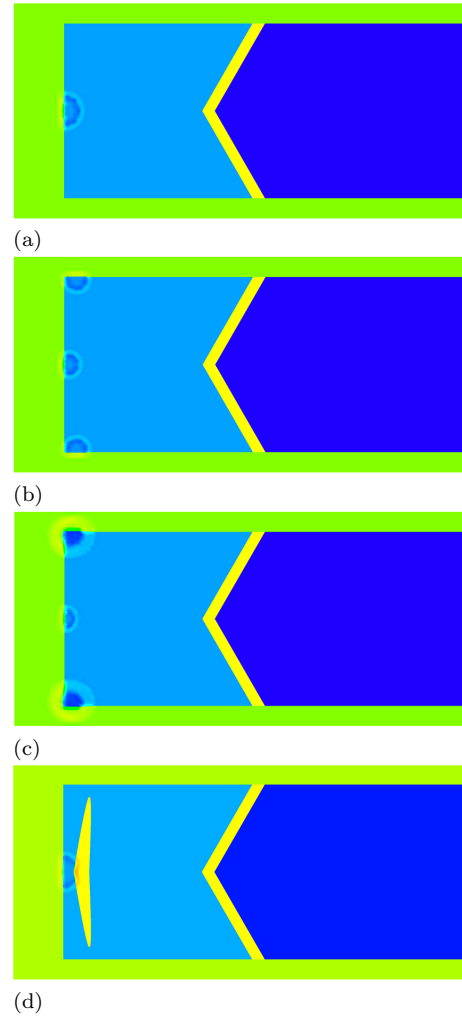

(a)

(b)

(c)

(d)

FIG. 9: Density plots at a time Δt just after detonator ignition for several cases that we investigated: (a) baseline case (see Figure 1), $\Delta t = 0.1$ μs; (b) optimal three detonators [see Figure 8(a)], $\Delta t = 0.1$ μs; (c) optimal three detonators with time delay [see Figure 8(b)], $\Delta t = 0.3$ μs; (d) optimal metal inclusion [see Figure 8(c)], $\Delta t = 0.1$ μs.

increasing the fitness metric Φ_2 for the optimal jet and consequently the penetration depth.

We also found that this optimal detonation wave front can be reproduced in a simpler manner by arraying three or more detonators along a specific function, such as a semicircle or parabola. For a semicircular arrangement, we refer to the center of the full circle as the focal point F, which corresponds to the semicircle radius (see Figure 13). Using the Merlin workflow software[49], we ran several sets of simulations using $N_d = 3$, 5, 7, and 60 detonators arrayed along a semicircle to investigate the effect of modifying F. For $N_d = 60$, the detonator array essentially produces a continuous detonation wave (see Figure 14). Figure 15 plots the fitness metric Φ_2 [see Equation (16)] versus F for several sets of simulations
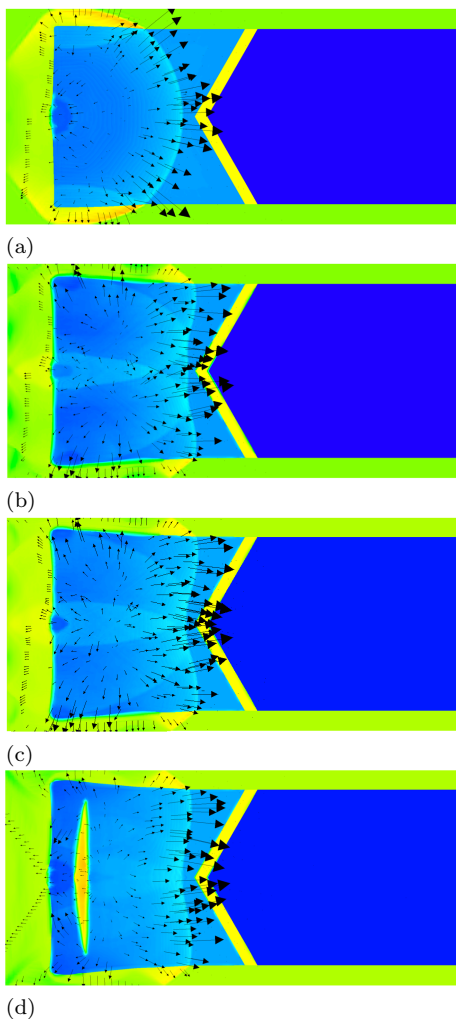
(a)

(b)

(c)

(d)

FIG. 10: Density plots at a time Δt just prior to the detonation wave striking the liner for several cases that we investigated. Velocity vectors (where size corresponds to magnitude) are overlaid on the plots to indicate the velocity direction of the detonation wave front: (a) baseline case (see Figure 1), $\Delta t = 1.4$ μs; (b) optimal three detonators [see Figure 8(a)], $\Delta t = 1.6$ μs; (c) optimal three detonators with time delay [see Figure 8(b)], $\Delta t = 1.7$ μs; (d) optimal metal inclusion [see Figure 8(c)], $\Delta t = 2.2$ μs.
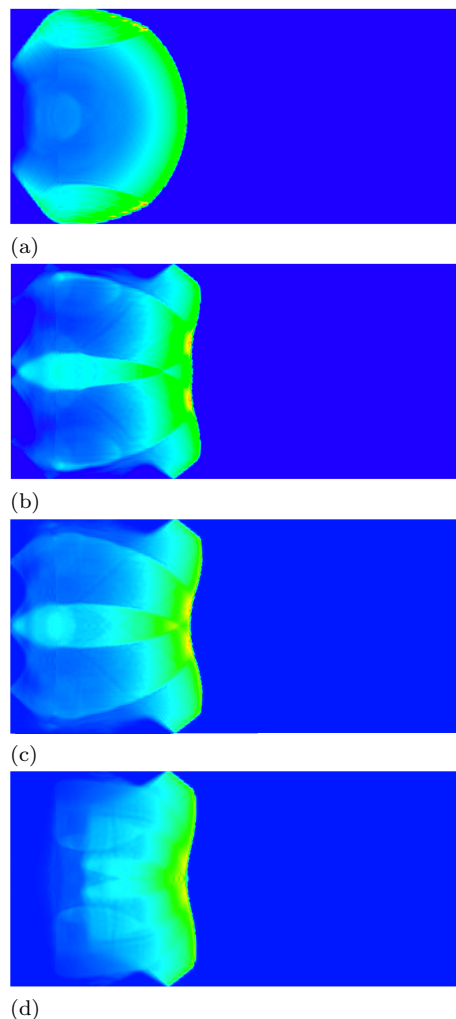

(a)

(b)

(c)

(d)

FIG. 11: Pressure plots at a time Δt just prior to the detonation wave striking the liner for several cases that we investigated: (a) baseline case (see Figure 1), $\Delta t = 1.4$ μs; (b) optimal three detonators [see Figure 8(a)], $\Delta t = 1.6$ μs; (c) optimal three detonators with time delay [see Figure 8(b)], $\Delta t = 1.7$ μs; (d) optimal metal inclusion [see Figure 8(c)], $\Delta t = 2.2$ μs.

involving different values of N_d. Figure 15(a), (b), and (c) are for cases where the liner angle $\alpha = 60°$, $45°$, and $30°$, respectively. Note that $F < 0$ implies that the array of detonators is convex and produces a convex detonation wave (similar to the baseline case) and $F > 0$ implies that the array of detonators is concave and produces a concave detonation wave. As the magnitude of F increases, the detonation wave becomes flatter.

The simulation data plotted in Figure 15 demonstrates that there is generally a distinct optimal value of F. As expected, the optimal value of F changes depending on the liner angle α that is used. For instance, for the case

where $\alpha = 30°$ and $N_d = 3$, the optimal value is $F \approx 3.6$ cm, whereas the optimal value is $F \approx 2.5$ cm for the case where $\alpha = 60°$ and $N_d = 3$. This optimal value of F also varies slightly as N_d is increased. For the optimal value, $F > 0$, which indicates that the optimal detonation wave front is slightly concave. This is consistent with the optimal detonation wave fronts produced from our other design parameterizations. Figure 14 shows the detonation wave prior to striking the target for the case where $F = 2.5$ cm, $N_d = 60$, and $\alpha = 60°$, which is clearly similar to the detonation wave fronts produced by our other optimal designs shown in Figures 10 and 11.

The natural question arises as to why these particular detonation wave fronts tend to optimize jetting. A partial answer to this question can be understood by consider-
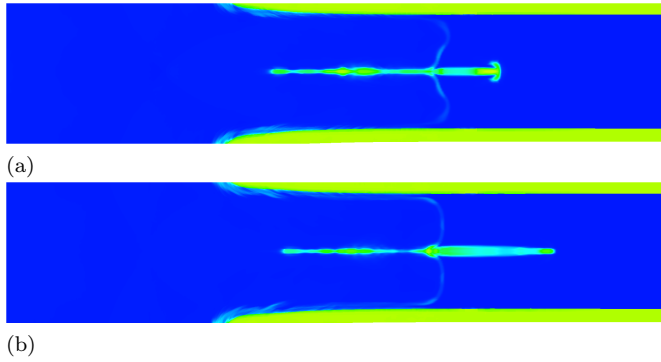
(a)

(b)

FIG. 12: Density plots showing the jet at $\Delta t = 15$ μs after detonator ignition for: (a) baseline case, jet tip velocity = 0.426 cm/μs; (b) optimal three detonator case [see Figure 8(a)], jet tip velocity = 0.465 cm/μs. Note that the jet for the optimal case has a higher tip velocity, with more mass concentrated towards the front of the jet where the jet material is moving fastest.
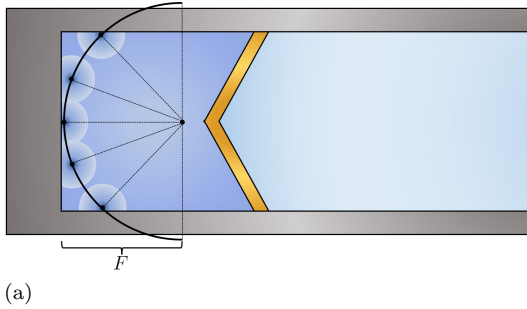

(a)

FIG. 13: A simplified design parameterization that involves only a single design parameter. The detonators are arrayed along a semicircle (spaced equidistantly in the y-direction). The detonation waves converge to a focal point F which corresponds to the radius of the circle. The diagram shows the case where the number of detonators $N_d = 5$ detonators, although any number of detonators can be used for this parameterization.

ing the diagrams in Figures 4 and 5. For a given liner collapse angle $\hat{\beta}$, we assume that there is a corresponding optimal collapse velocity v_0 that will produce values of v_j and m_j that correspond to an optimal fitness metric [e.g., the metric Φ_2 in Equation (16)]. Since $\hat{\beta}$ is not constant and varies as the detonation wave sweeps across the liner, the optimal collapse velocity v_0 will also vary over time. By tuning the incidence angle of the detonation wave ω, which corresponds to the shape of the detonation wave front, we can ideally ensure that we obtain the optimal collapse velocity v_0 at all times because v_0 is directly dependent on ω via Equation (5). We note that altering the type of HE used or making minor modifications to the liner geometry could alter the values of the optimal parameters needed to achieve an optimal detonation wave front. For instance, using a different type of
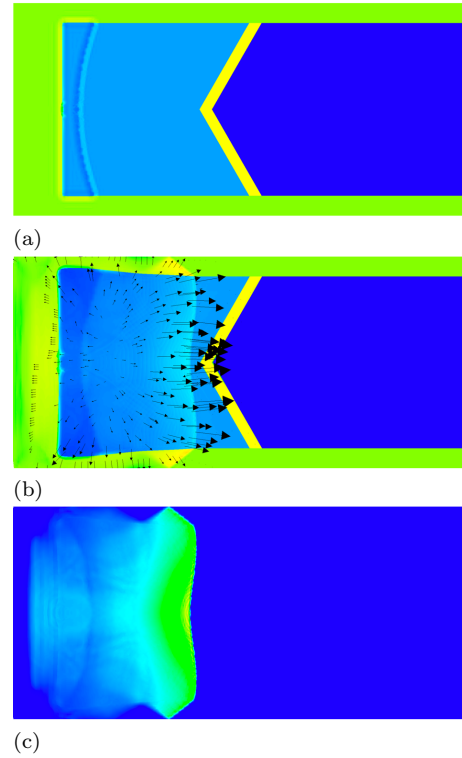

(a)

(b)

(c)

FIG. 14: Density and pressure plots for a semicircle detonator configuration where $F = 2.5$ cm, $N_d = 60$, and $\alpha = 60°$. The detonation wave front is shown at an early time and at a time just prior to striking the liner: (a) density, $\Delta t = 0.1$ μs; (b) density with velocity vectors, $\Delta t = 1.3$ μs; (c) pressure, $\Delta t = 1.3$ μs.

HE would affect the detonation velocity and would likely require modifying the detonator locations to reproduce the optimal detonation wave front.

The plots in Figure 15 also appear to demonstrate that the pressure increase from detonation wave collisions (P_2/P_1 as described in Appendix A) are having a relatively minor effect on our fitness metric Φ_2 and consequently the penetrative properties of the jet. As the number of detonators N_d along the semicircular array is increased, the point detonators tend to blend into a single continuous line and there are essentially no detonation wave collisions induced between the detonation waves emanating from the individual point detonators. Figure 15 demonstrates that, for $N_d = 60$ where detonation wave collisions are negligible, there is very little change in Φ_2 from the simulations that use $N_d = 5$ where detonation wave collisions are induced. This is a surprising result and appears to indicate that these detonation wave collisions have a less significant effect on the jetting properties than the angle ω at which the detonation wave strikes the liner.
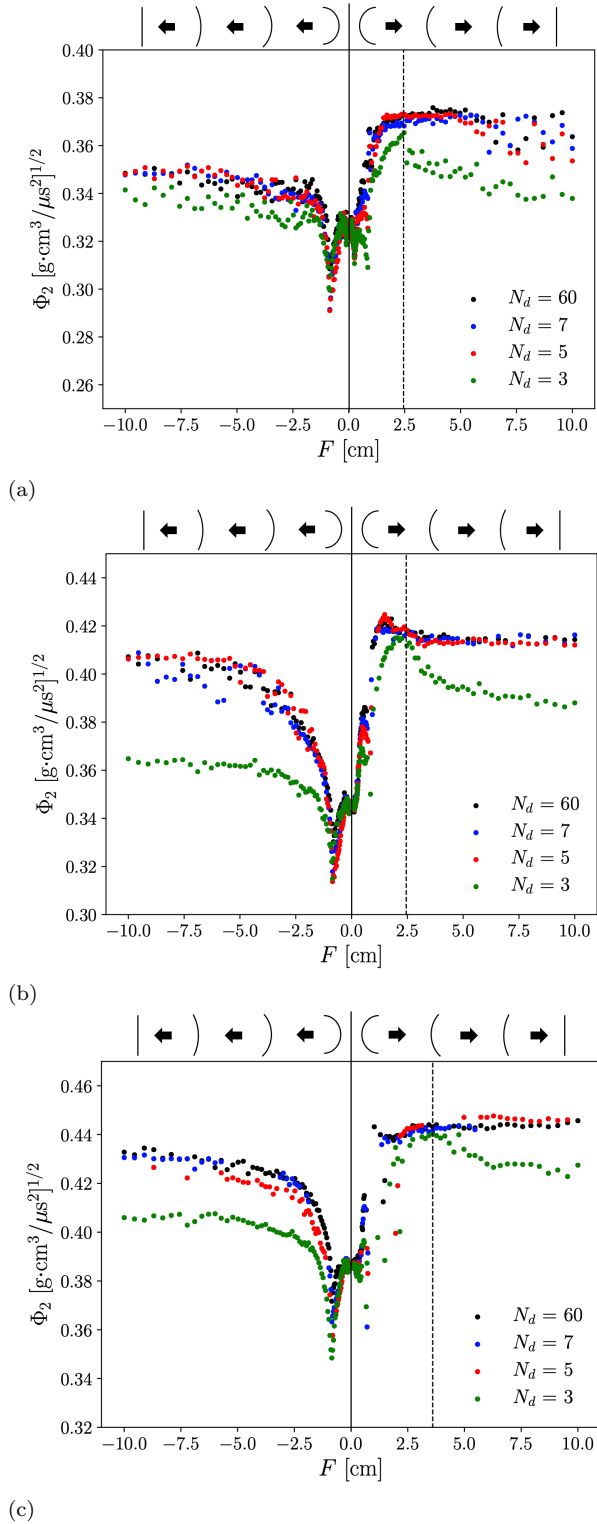
(a)

(b)

(c)

FIG. 15: The fitness metric Φ_2 plotted versus the parameter F for several detonator quantities (i.e., $N_d = 3, 5, 7$ and 60). The liner angle α is varied for each plot in the figure: (a) $\alpha = 60°$; (b) $\alpha = 45°$; (c) $\alpha = 30°$. The relative concavity versus convexity for values of F are marked above each plot (these markings are meant to indicate the general behavior and are not drawn to scale). The vertical solid line indicates where $F = 0$ and the vertical dashed line approximately corresponds to the optimal F for $N_d = 3$.

IV. CONCLUSIONS

Our optimization study demonstrates that there is an optimal detonation wave front profile that increases the penetration depth of the shaped-charge jet into a given material. We were able to reproduce this detonation wave front profile using several different parameterizations that involve modifying the locations of multiple detonators, the time delay between detonators, and using a metal inclusion within the HE region. The fact that we are able to arrive at very similar optimal detonation wave fronts indicates a "convergent evolution" effect and implies that we have obtained a fairly optimal point in the parameter search spaces that we considered.

The collisions between detonation waves is another phenomenon that we investigated in our study. Using our design parameterizations, we are able to instigate collisions between detonation waves, which increases the pressure in the collision region between the waves. We had originally hypothesized that the localized pressure increases due to detonation wave collisions may help to increase jet velocity and penetration depth. However, we found that the shape of the detonation wave profile appeared to be a much more significant factor in optimizing the linear shaped charge jetting than these localized pressure increases from detonation wave collisions.

Future work may involve applying some of the lessons learned in this study to other linear shaped-charge geometries. This includes modifying liner properties to observe the effect that this has on the optimal detonation wave front. Experimental studies may also provide some additional insight and provide a means of validating the optimal designs that we developed in this study.

ACKNOWLEDGMENTS

AUTHOR DECLARATIONS

Conflict of Interest

The authors have no conflicts to disclose.

DATA AVAILABILITY

The data that support the findings of this study are available from the corresponding author upon reasonable

request.

Appendix A: Detonation wave collisions

Most shape charge designs involve a single detonator or a single line of detonators that create a single detonation wave that interacts with the liner material. However, the collision between multiple detonation waves initiated from separate detonators can increase pressure in the collision region between the detonation waves above the pressure of the individual waves, which we hypothesized could be used to enhance the kinetic energy of the jet. In the following paragraphs we use the Rankine–Hugoniot equations to derive the bounds on this pressure increase and its relational dependence on the angle at which the detonation waves collide (i.e., the incidence angle). We begin by considering the symmetric collision of two detonation waves in two dimensions as shown in Figure 16.
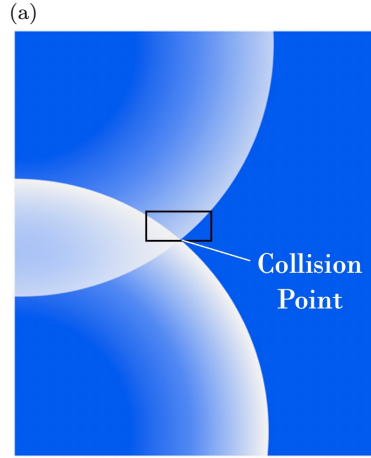
When two detonation waves collide, the detonation wave front behind the collision point is converted to a shock wave that traverses the products that have been reacted by the opposing detonation wave. This causes a refractive effect as the shock wave is not self-sustaining and is moving through a new medium (i.e., the reacted products rather than the reactants through which the detonation waves move). The collision of two detonation waves creates three distinct regions, which are the undetonated region ahead of the detonation wave (Region 0), the region behind each detonation wave (Region 1, which excludes the collision region), and the collision region (Region 2) between the two detonation waves [see Figures 16(b) and 17]. We denote properties of these regions using the subscripts 0, 1, and 2, respectively.

Following the methodology described by Zhang et al.[25], Bdzil and Short[52], Zhang[24], and Liu et al.[13], we can approximate the behavior within the three regions of the box shown in Figure 16(b) (i.e., the three regions near the collision point) as being equivalent to the stationary reflection of an oblique detonation wave at a rigid wall where the reflected wave is a shock wave. Under this approximation, we can describe the behavior in the three regions using the diagram of Figure 17. Regions 0 and 1 are separated by the incident oblique detonation wave with angle ϕ_0 and Regions 1 and 2 are separated by the reflected shock wave with angle ϕ_2. Due to the refractive effect, the angle of incidence ϕ_0 is generally not equal to the angle of reflection ϕ_2. Note that the velocity at which mass enters perpendicularly to the stationary oblique detonation wave is equal to the detonation wave velocity u_d in this approximation. In the following paragraphs, we develop a relation for the ratio of the pressure near the collision point in the collision region to the pressure of the individual detonation waves (i.e., P_2/P_1) as a function of the incidence angle ϕ_0.

We start this derivation using a similar process to that described by Zhang et al.[25]. The Rankine–Hugoniot con-

Detonator Location

(a)

Collision Point
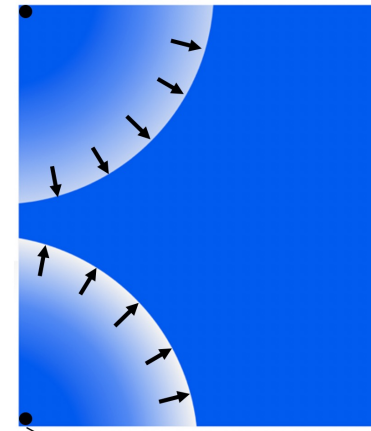
(b)

FIG. 16: When two detonation waves collide, a high-pressure area is created in the region in which the detonation waves overlap: (a) prior to detonation wave collision; (b) just after the detonation waves collide. The black rectangle shown in (b) represents the three regions we consider in Figure 17.

servation of mass equation applied across Regions 1 and 2 is equal to

$$\rho_1 u_{1,n} = \rho_2 u_{2,n}, \qquad (A1)$$

where ρ is density and u is the velocity of the mass within the specified region relative to the oblique detonation wave or the reflected shock wave. The subscripts n and t denote the normal and tangential components of velocity relative to the oblique detonation wave (or the reflected shock wave), respectively. The normal component of velocity for mass in Region 1 that is entering Region 2 (i.e., $u_{1,n}$) can be found from the following geometric relation

$$u_{1,n} = u_1 \sin(\phi_2 + \theta), \qquad (A2)$$

where θ represents the deflection angle of the mass as it passes through the reflected shock wave and ϕ_2 is the
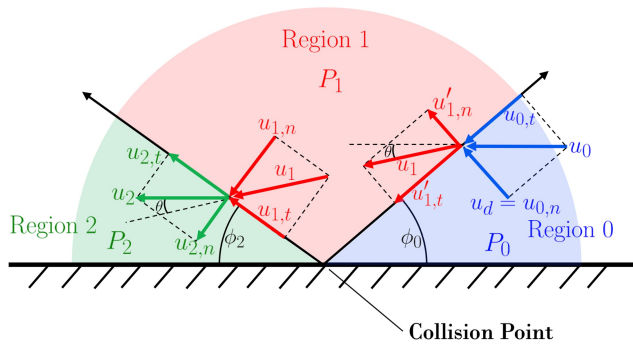
(a)

FIG. 17: The collision of two symmetrical detonation waves can be approximated as a detonation wave reflecting off of a rigid wall[13,24,25]. Under this approximation, there are three regions to consider: Region 0 represents the undetonated region, Region 1 is the region behind the detonation wave (excluding the collision region), and Region 2 is the collision region. The variables used in the derivation for the ratio of pressures between Region 2 and Region 1 (i.e., P_2/P_1) are marked on the diagram.

angle of reflection (see Figure 17). Substituting Equation (A2) into (A1) and rearranging, we obtain the following relation for $u_{2,n}$:

$$u_{2,n} = \frac{\rho_1}{\rho_2} \sin(\phi_2 + \theta). \tag{A3}$$

We now consider the Rankine–Hugoniot conservation of momentum equation across Regions 1 and 2, which is equal to

$$P_1 + \rho_1 u_{1,n}^2 = P_2 + \rho_2 u_{2,n}^2. \tag{A4}$$

After some minor rearrangement and using the conservation of momentum, where $\rho_1 u_{1,n} = \rho_2 u_{2,n}$, Equation (A4) can be rewritten as

$$P_2 - P_1 = \rho_1 u_{1,n}(u_{1,n} - u_{2,n}). \tag{A5}$$

Substituting Equations (A2) and (A3) into (A5) allows us to eliminate $u_{2,n}$ from the expression to produce

$$P_2 - P_1 = \rho_1 u_1 \sin(\phi_2 + \theta)[u_1 \sin(\phi_2 + \theta) - \frac{\rho_1}{\rho_2} u_1 \sin(\phi_2 + \theta)], \tag{A6}$$

which can be further rearranged to obtain

$$\frac{P_2}{P_1} = 1 + \frac{\rho_1 u_1^2}{P_1}\left(1 - \frac{\rho_1}{\rho_2}\right)\sin^2(\phi_2 + \theta). \tag{A7}$$

The density ratio across the reflected shock wave [i.e., ρ_1/ρ_2 in Equation (A7)] can be developed using the Rankine–Hugoniot equations for the conservation of mass, momentum, and energy (a derivation of the following equation is provided in many textbooks on the

subject[53]) and is equal to

$$\frac{\rho_1}{\rho_2} = \frac{2 + (\gamma - 1)M_n^2}{(\gamma + 1)M_n^2}, \tag{A8}$$

where $M_n = M \sin(\phi_2 + \theta)$ is the Mach number normal to the reflected shock wave separating Regions 1 and 2.

The Mach number M can be derived in the following way. By definition, the velocity u_1 is equal to (see Figure 17)

$$u_1 = \left[u_{1,n}'^2 + u_{1,t}'^2\right]^{1/2}. \tag{A9}$$

According to the Chapman–Jouguet condition, which assumes that the detonation wave just reaches the speed of sound c_1, the normal velocity is equal to

$$u_{1,n}' = c_1 = \frac{\gamma}{\gamma + 1} u_d, \tag{A10}$$

and, from trigonometry, the tangential velocity is equal to

$$u_{1,t}' = u_{0,t} = \frac{u_d}{\tan(\phi_0)}. \tag{A11}$$

Substituting the relations in Equations (A10) and (A11) into Equation (A9) and performing some minor algebra produces[13,25]

$$M = \frac{u_1}{c_1} = \left[1 + \left(\frac{\gamma + 1}{\gamma}\right)^2 \cot^2(\phi_0)\right]^{1/2}, \tag{A12}$$

which allows us to compute the Mach number M as a function of only the incidence angle ϕ_0 and the ratio of specific heats γ of the HE.

Additionally, the material equation of state (EOS) for the HE can be used to calculate the ratio ρ_1/P_1 in the second term on the right-hand side of Equation (A7). For this derivation, we assume that the HE EOS can be described simply as[25]

$$\frac{\rho_1}{P_1} = \frac{\gamma}{c_1^2}. \tag{A13}$$

Using the definition of the Mach number (i.e., $M = u_1/c_1$), we can rewrite Equation (A13) as

$$\frac{\rho_1}{P_1} = \frac{\gamma M^2}{u_1^2}. \tag{A14}$$

If we now substitute Equations (A8) and (A14) into Equation (A7), we obtain the following expression:

$$\frac{P_2}{P_1} = \frac{(1 - \gamma)}{\gamma + 1} + \frac{2\gamma}{(\gamma + 1)} M^2 \sin^2(\phi_2 + \theta). \tag{A15}$$

Equations (A12) and (A15) provide an explicit relation for the pressure ratio P_2/P_1 as a function of only the ratio of specific heats γ, the deflection angle θ, the incidence angle ϕ_0, and the reflection angle ϕ_2. Note that for many

types of explosives, $\gamma \in [2,3]$ and is dependent on the explosive material that is used.

To develop a relation solely between P_2/P_1 and the incidence angle ϕ_0, we must first find expressions that relate θ and ϕ_2 to ϕ_0. We start by deriving an expression relating θ and ϕ_0. The following relation can be derived from basic trigonometry:

$$\tan(\phi_0 - \theta) = \frac{u'_{1,n}}{u'_{1,t}}. \tag{A16}$$

Substituting Equations (A10) and (A11) into Equation (A16) produces

$$\tan(\phi_0 - \theta) = \frac{\gamma}{\gamma + 1} \tan(\phi_0), \tag{A17}$$

which can be further simplified using the well-known trigonometric relation:

$$\tan(\phi_0 - \theta) = \frac{\tan(\phi_0) - \tan(\theta)}{1 + \tan(\phi_0)\tan(\theta)}. \tag{A18}$$

Setting Equations (A17) and (A18) equal to each other and solving for θ gives the following explicit expression for computing θ as a function of only ϕ_0:

$$\theta = \tan^{-1}\left\{\frac{\tan(\phi_0)}{1 + \gamma\left[1 + \tan^2(\phi_0)\right]}\right\}. \tag{A19}$$

To develop a relation between ϕ_2 and ϕ_0, we again apply the Rankine–Hugoniot conservation of mass across Regions 1 and 2, such that

$$\frac{u_{2,n}}{u_{1,n}} = \frac{\rho_1}{\rho_2}. \tag{A20}$$

From simple geometry, the normal and tangential velocity components are equal to

$$\begin{aligned} u_{1,n} &= u_1 \sin(\phi_2 + \theta), \\ u_{1,t} &= u_1 \cos(\phi_2 + \theta), \\ u_{2,n} &= u_2 \sin(\phi_2), \\ u_{2,t} &= u_2 \cos(\phi_2). \end{aligned} \tag{A21}$$

Dividing the normal and tangential velocity components of Equation (A21) produces

$$\frac{u_{1,n}}{u_{1,t}} = \frac{u_1 \sin(\phi_2 + \theta)}{u_1 \cos(\phi_2 + \theta)} = \tan(\phi_2 + \theta), \tag{A22}$$

and

$$\frac{u_{2,n}}{u_{2,t}} = \frac{u_2 \sin(\phi_2)}{u_2 \cos(\phi_2)} = \tan(\phi_2). \tag{A23}$$

From the conservation of momentum, the tangential components of velocity that act along the reflected shock wave are equal (i.e., $u_{1,t} = u_{2,t}$). Using this fact and

dividing Equation (A23) by Equation (A22), we obtain the following relation

$$\frac{u_{2,n}}{u_{1,n}} = \frac{\tan(\phi_2)}{\tan(\phi_2 + \theta)} = \frac{\rho_1}{\rho_2}, \tag{A24}$$

which is equal to the density ratio ρ_1/ρ_2 according to Equation (A20). Setting Equation (A24) equal to Equation (A8) results in

$$\frac{\tan(\phi_2)}{\tan(\phi_2 + \theta)} = \frac{2 + (\gamma - 1)[M \sin(\phi_2 + \theta)]^2}{(\gamma + 1)[M \sin(\phi_2 + \theta)]^2}, \tag{A25}$$

which provides an implicit relation between ϕ_2 and θ that is only a function of γ and M.

By simultaneously solving the implicit relation in Equations (A25) and the expressions in Equations (A12), (A15), and (A19), we can compute the pressure ratio P_2/P_1 as a function of only the incidence angle ϕ_0 and the ratio of specific heats γ (which is a material property of the HE through which the detonation waves are propagating). Figure 18(a) provides a plot of P_2/P_1 versus the incidence angle ϕ_0 for several values of $\gamma \in [2,3]$. Similarly, Figure 18(b) provides a plot of θ versus the incidence angle ϕ_0 for several γ values. According to Bdzil and Short[52], there is a critical incidence angle $\phi_{0,c}$ (generally between $40°$ and $50°$) above which the reflected shock wave becomes irregular. At this point, the assumption that the velocity u_2 is parallel to the rigid wall breaks down and the formulation described above is no longer valid. For $\phi_0 > \phi_{0,c}$, the collision point tracks along a line rather than a single point. The plots in Figure 18 are only plotted up to this critical incidence angle $\phi_{0,c}$.
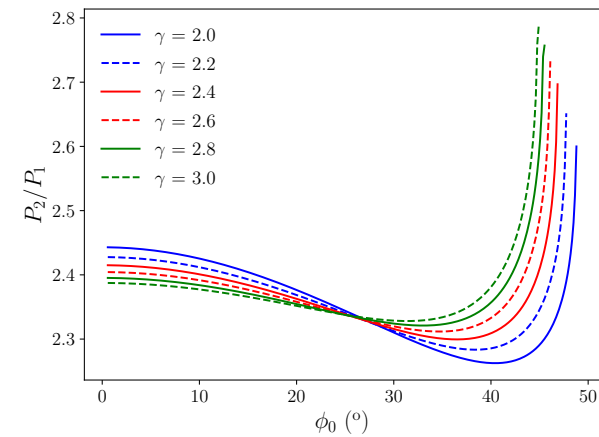
An approximate alternative formulation that may be useful for some applications is to assume that the detonation waves near the collision point partially behave in a similar manner to shock waves. For this approximate formulation, the following relation could be used in place of Equation (A19) to determine θ:

$$\frac{\tan(\phi_0 - \theta)}{\tan(\phi_0)} = \frac{2 + (\gamma - 1)[M \sin(\phi_0)]^2}{(\gamma + 1)[M \sin(\phi_0)]^2}, \tag{A26}$$
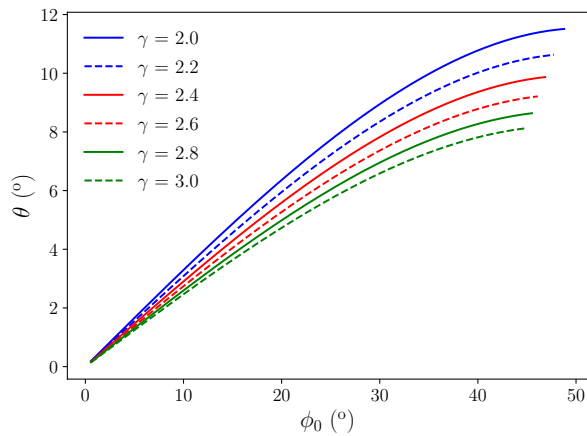
which can be derived in a similar way to Equation (A25) by applying the same method across Regions 0 and 1. Figure 19 shows a plot of P_2/P_1 for this alternative formulation. In this case, the maximum pressure increase P_2/P_1 that is achievable from the collision of two detonation waves occurs when the incidence angle $\phi_0 = 0$ (i.e., when the detonation waves strike each other head on) and decreases to unity as $\phi_0 \to \pi/2$ (i.e., when the detonation waves are moving parallel to each other). This approximate alternative formulation may be useful in some cases.

[1] P. De Frank, Explosive technology meets North Sea challenge, J. Pet. Technol. 20 (02) (1968) 121–124.
[2] P.-A. Persson, R. Holmberg, J. Lee, Rock blasting and explosives engineering, CRC press, 2018.

(a)

(b)

FIG. 18: The pressure ratio P_2/P_1 and deflection angle θ can be computed as a function of the incidence angle ϕ_0 using Equations (A15) and (A19), respectively: (a) pressure ratio P_2/P_1 versus ϕ_0; (b) deflection angle θ versus ϕ_0.

(a)

FIG. 19: The pressure ratio P_2/P_1 as a function of the incidence angle ϕ_0 using Equation (A15) where Equation (A26) is used to compute θ.

Phys. Fluids 34 (8) (2022) 082109.

[10] G. Birkhoff, D. P. MacDougall, E. M. Pugh, S. G. Taylor, Explosives with lined cavities, J. Appl. Phys. 19 (6) (1948) 563–582.

[11] E. M. Pugh, R. Eichelberger, N. Rostoker, Theory of jet formation by charges with lined conical cavities, J. Appl. Phys. 23 (5) (1952) 532–536.

[12] Z. Wang, J.-W. Jiang, S.-Y. Wang, H. Liu, Jet formation and penetration study of double-layer shaped charge, J. Energetic Mater. 36 (2) (2018) 152–168.

[13] Y. Liu, J. Yin, Z. Wang, Study on the overdriven detonation wave propagation in double-layer shaped charge, Phys. Fluids 31 (9) (2019) 092110.

[14] Y. Liu, J. Yin, Z. Wang, Study on overdriven detonation of double-layer shaped charge, Propellants Explos. Pyrotech. 44 (11) (2019) 1410–1422.

[15] D. Pyka, A. Kurzawa, M. Bocian, M. Bajkowski, M. Magier, J. Sliwinski, K. Jamroziak, Numerical and experimental studies of the ŁK type shaped charge, Appl. Sci. 10 (19) (2020) 6742.

[16] Y. Liu, J. Yin, Z. Wang, X. Zhang, G. Bi, The efp formation and penetration capability of double-layer shaped charge with wave shaper, Materials 13 (20) (2020) 4519.

[17] Y. Wu, C. Chen, et al., Detonation wave propagation of double-layer shaped charge and its driving characteristics to the liner, Shock and Vib. 2023.

[18] M. J. Murphy, R. M. Kuklo, Fundamentals of shaped charge penetration in concrete, in: 18th international symposium on ballistics, San Antonio, Texas, 1999.

[19] C. Wang, T. Ma, J. Ning, Experimental investigation of penetration performance of shaped charge into concrete targets, Acta Mech. Sin. 24 (3) (2008) 345–349.

[20] Z. Zhang, L. Wang, V. V. Silberschmidt, Damage response of steel plate to underwater explosion: Effect of shaped charge liner, Int. J. Impact Eng. 103 (2017) 38–49.

[21] X. Cheng, G. Huang, C. Liu, S. Feng, Design of a novel linear shaped charge and factors influencing its penetration performance, Appl. Sci. 8 (10) (2018) 1863.

[22] G. Ma, G. He, Numerical simulation and experimental study on shaped charge warhead of guided ammunition, Shock Vib. 2021 (2021) 1–15.

[23] W. Xu, C. Wang, J. Yuan, Impact performance of an annular shaped charge designed by convolutional neural networks, Thin-Walled Struct. 160 (2021) 107241.

[24] S. Zhang, Explosion and impact dynamics, Weapon Industry Press (1993) 74–78.

[3] Y.-H. Ko, S.-J. Kim, H.-S. Yang, Assessment for the sympathetic detonation characteristics of underwater shaped charge, Geosyst. Eng. 20 (5) (2017) 286–293.

[4] L. Cheng, C. Ji, M. Zhong, Y. Long, F. Gao, Full-scale experimental investigation on the shock-wave characteristics of high-pressure natural gas pipeline physical explosions, Int. J. Hydrogen Energy 44 (36) (2019) 20587–20597.
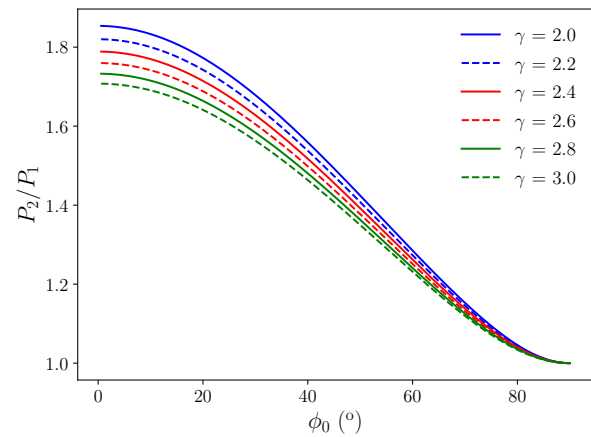
[5] J. Sun, Z. Ma, Z. Zhang, F. Weng, R. Chen, The delamination of carbon fiber reinforced composites during cutting by flexible linear shaped charge, J. Mech. Sci. Technol. 34 (2020) 1515–1522.

[6] S. Choi, S. Kwon, S.-E. Lee, M.-A. Moon, Shock response of precision linear shaped charge in a multistage rocket system, Int. J. Aeronaut. Space Sci. (2022) 1–13.

[7] N. J. Zabusky, Vortex paradigm for accelerated inhomogeneous flows: Visiometrics for the Rayleigh–Taylor and Richtmyer–Meshkov environments, Annu. Rev. Fluid Mech. 31 (1) (1999) 495–536.

[8] M. Brouillette, The Richtmyer–Meshkov instability, Annu. Rev. Fluid Mech. 34 (1) (2002) 445–468.

[9] D. M. Sterbentz, C. F. Jekel, D. A. White, S. Aubry, H. E. Lorenzana, J. L. Belof, Design optimization for Richtmyer–Meshkov instability suppression at shock-compressed material interfaces,

[25] K. Zhang, M. Liang, F. Lu, X. Li, Mechanics of plate fracture from detonation wave interaction, Propellants Explos. Pyrotech. 44 (2) (2019) 188–197.

[26] M. E. Backman, W. Goldsmith, The mechanics of penetration of projectiles into targets, Int. J. Eng. Sci. 16 (1) (1978) 1–99.

[27] R. Anderson, A. Black, B. Blakeley, R. Bleile, J.-S. Camier, J. Ciurej, A. Cook, V. Dobrev, N. Elliott, J. Grondalski, C. Harrison, R. Hornung, T. Kolev, M. Legendre, W. Liu, W. Nissen, B. Olson, M. Osawe, G. Papadimitriou, O. Pearce, R. Pember, A. Skinner, D. Stevens, T. Stitt, L. Taylor, V. Tomov, R. Rieben, A. Vargas, K. Weiss, D. White, L. Busby, The multiphysics on advanced platforms project, Tech. Rep. Tech. rep., LLNL-TR-815869, Lawrence Livermore National Laboratory, Livermore, CA (United States) (2020). `doi:10.2172/1724326`.

[28] R. Rieben, Poster: The MARBL multi-physics code, in: Exascale Computing Project Annual Meeting, 2020. `doi:10.13140/RG.2.2.12326.14403`.

[29] R. W. Anderson, V. A. Dobrev, T. V. Kolev, R. N. Rieben, V. Z. Tomov, High-order multi-material ALE hydrodynamics, SIAM J. Sci. Comput. 40 (1) (2018) B32–B58.

[30] M. Larsen, E. Brugger, H. Childs, C. Harrison, Ascent: A Flyweight In Situ Library for Exascale Simulations, in: In Situ Visualization For Computational Science, Mathematics and Visualization book series from Springer Publishing, Cham, Switzerland, 2022, pp. 255 – 279.

[31] D. A. Young, Phase diagrams of the elements, University of California Press, 1991.

[32] R. More, K. Warren, D. Young, G. Zimmerman, A new quotidian equation of state (QEOS) for hot dense matter, Phys. Fluids 31 (10) (1988) 3059–3078. `doi:10.1063/1.866963`.

[33] D. A. Young, E. M. Corey, A new global equation of state model for hot, dense matter, J. Appl. Phys. 78 (6) (1995) 3748–3755. `doi:10.1063/1.359955`.

[34] D. Steinberg, S. Cochran, M. Guinan, A constitutive model for metals applicable at high-strain rate, J. Appl. Phys. 51 (3) (1980) 1498–1504.

[35] S. Cochran, J. Chan, Shock initiation and detonation models in one and two dimensions.[PBX-9404, RX-03-BB], Tech. rep., California Univ., Livermore (USA). Lawrence Livermore Lab. (1979).

[36] E. L. Lee, C. M. Tarver, Phenomenological model of shock initiation in heterogeneous explosives, The Physics of Fluids 23 (12) (1980) 2362–2372.

[37] S. Cochran, C. Tarver, Modeling particle size and initial temperature effects on shock initiation of TATB-based explosives, in: Shock Waves in Condensed Matter 1983, Elsevier, 1984, pp. 593–596.

[38] V. Dobrev, F. Grogan, T. Kolev, R. Rieben, V. Tomov, Level set methods for detonation shock dynamics using high-order finite elements, Tech. rep., Lawrence Livermore National Laboratory (LLNL), Livermore, CA (United States) (2017).

[39] C. Handley, B. Lambourn, N. Whitworth, H. James, W. Belfield, Understanding the shock and detonation response of high explosives at the continuum and meso scales, Applied Physics Reviews 5 (1) (2018) 011303.

[40] M. L. Combrinck, T. Gadal, A. Hargreaves, J. E. Martin, Velocity tracking of shaped charge wire formation and propagation toward the target, J. Energetic Mater. (2022) 1–20.

[41] W. P. Walters, W. Flis, P. Chou, A survey of shaped-charge jet penetration models, Int. J. Impact Eng. 7 (3) (1988) 307–325.

[42] T. Elshenawy, A. Elbeih, Q. Li, Influence of target strength on the penetration depth of shaped charge jets into RHA targets, Int. J. Mech. Sci. 136 (2018) 234–242.

[43] K. K. Vu, C. D'Ambrosio, Y. Hamadi, L. Liberti, Surrogate-based methods for black-box optimization, Int. Trans. Op. Res. 24 (2017) 393–424.

[44] D. R. Jones, A taxonomy of global optimization methods based on response surfaces, J. Global Optimization 21 (2001) 345–383.

[45] S. Koziel, Y.-S. Yang, Computational optimization, methods and algorithms, Springer, 2011.

[46] J. Jones, A. E. Eiben, T. Bartz-Bielstein, A new taxonomy of global optimization algorithms, Nat. Comput. 21 (2022) 219–242.

[47] N. V. Queipo, R. T. Haftka, W. Shyy, T. Goel, R. Vaidyanathan, P. K. Tucker, Surrogate-based analysis and optimization, Prog. Aerosp. Sci. 41 (1) (2005) 1–28.

[48] D. A. White, W. J. Arrighi, J. Kudo, S. E. Watts, Multiscale topology optimization using neural network surrogate models, Comput. Methods Appl. Mech. Eng. 346 (2019) 1118–1135.

[49] L. Petersen, et. al., Enabling machine learning-ready HPC ensembles with Merlin, Future Gener. Comput. Syst. 131 (2022) 255–268.

[50] Pytorch, https://www.pytorch.org, accessed 2023-03-08.

[51] LLNL HPC: Lassen, https://hpc.llnl.gov/hardware/compute-platforms/lassen, accessed 2023-04-06.

[52] J. B. Bdzil, M. Short, Theory of Mach reflection of detonation at glancing incidence, Journal of Fluid Mechanics 811 (2017) 269–314.

[53] M. J. Zucrow, J. D. Hoffman, Gas dynamics: Volume 1, Cambridge University Press, New York, 1976.